Article

SOURCE DATA

TRANSPARENT PROCESS

EMBO *reports*

Structural basis for receptor recognition and pore formation of a zebrafish aerolysin-like protein

Ning Jia[1], Nan Liu[2], Wang Cheng[1], Yong-Liang Jiang[1], Hui Sun[1], Lan-Lan Chen[1], Junhui Peng[1], Yonghui Zhang[1], Yue-He Ding[3], Zhi-Hui Zhang[1], Xuejuan Wang[1], Gang Cai[1], Junfeng Wang[4], Meng-Qiu Dong[3], Zhiyong Zhang[1], Hui Wu[5], Hong-Wei Wang[2,*], Yuxing Chen[1,**] & Cong-Zhao Zhou[1,***]

Abstract

Various aerolysin-like pore-forming proteins have been identified from bacteria to vertebrates. However, the mechanism of receptor recognition and/or pore formation of the eukaryotic members remains unknown. Here, we present the first crystal and electron microscopy structures of a vertebrate aerolysin-like protein from *Danio rerio*, termed Dln1, before and after pore formation. Each subunit of Dln1 dimer comprises a β-prism lectin module followed by an aerolysin module. Specific binding of the lectin module toward high-mannose glycans triggers drastic conformational changes of the aerolysin module in a pH-dependent manner, ultimately resulting in the formation of a membrane-bound octameric pore. Structural analyses combined with computational simulations and biochemical assays suggest a pore-forming process with an activation mechanism distinct from the previously characterized bacterial members. Moreover, Dln1 and its homologs are ubiquitously distributed in bony fishes and lamprey, suggesting a novel fish-specific defense molecule.

Introduction

Pore-forming proteins (PFPs) have been identified in various organisms from all kingdoms of life [1]. They are powerful biological weapons that kill target cells by forming transmembrane pores for different purposes, including defense, attack, and/or signaling [1].

They are usually synthesized as a water-soluble pre-form protein, which is able to oligomerize into a ring-like complex that penetrates the target cell membrane, leading to the leakage of intracellular matrix and eventually the death of the target cell [2]. The well-characterized bacterial PFPs are able to kill the host cells and/or other species of bacteria [2], thereby also termed pore-forming toxins (PFTs). Based on the secondary structure elements that insert into the target membrane, bacterial PFTs have been classified into two groups: α and β-PFTs [3]. The latter, which represents the majority of characterized PFTs, covers three main families: the cholesterol-dependent cytolysin (CDC), staphylococcal α-toxin, and aerolysin [3].

In contrast to bacterial PFTs, the eukaryotic PFPs exhibit very diversified functions. For example, human apoptosis-related Bcl2-like proteins form pores on mitochondrial outer membrane [4], whereas the amyloid-forming proteins may form pores on human neuronal membrane, leading to the death of neurons and eventually neurodegenerative diseases [5]. In addition, the mammal PFP perforin-2, which is homologous to bacterial CDCs, is involved in the defense against microbes [6]. Recently, six new members of aerolysin family have been identified from eukaryotes: the mushroom *Laetiporus sulphureus* lectin (LSL) [7], the Brazilian tree *Enterolobium contortisiliquum* enterolobin [8], the green hydra *Chlorohydra viridissima* hydralysins [9], the earthworm *Eisenia foetida* lysenin [10], the snail *Biomphalaria glabrata* biomphalysin [11], and the frog *Bombina maxima* βγ-CAT [12]. These eukaryotic aerolysin members either serve as defense molecules to fight against pathogens or parasites [11,12] or assist the animal in prey disintegration as in the case of hydralysins [13].

In past decades, the water-soluble pre-form structures of a lot of prokaryotic aerolysin members [14,15] and two eukaryotic members [7,10] have been reported. Structural analyses indicated that they all share a conserved aerolysin fold, usually fused with various receptor-binding domains (RBDs). The RBD determines the

1 Hefei National Laboratory for Physical Sciences at the Microscale and School of Life Sciences, University of Science and Technology of China, Hefei, China
2 Ministry of Education Key Laboratory of Protein Science, Tsinghua-Peking Joint Center for Life Sciences, Center for Structural Biology, School of Life Sciences, Tsinghua University, Beijing, China
3 National Institute of Biological Sciences, Beijing, China
4 High Magnetic Field Laboratory, Hefei Institutes of Physical Science, Chinese Academy of Sciences, Hefei, China
5 Departments of Microbiology and Pediatric Dentistry, Schools of Dentistry and Medicine, University of Alabama at Birmingham, Birmingham, AL, USA
*Corresponding author. Tel: +86 10 62798651; E-mail: hongweiwang@tsinghua.edu.cn
**Corresponding author. Tel: +86 551 63602492; E-mail: cyxing@ustc.edu.cn
***Corresponding author. Tel: +86 551 63600406; E-mail: zcz@ustc.edu.cn

specificity toward the target cell, whereas the aerolysin fold contributes to the pore formation [14]. To date, most structural information for the oligomeric pre-pore/pore state and related conformational changes are restricted in the bacterium *Aeromonas hydrophila* aerolysin [16]. It is synthesized and initially secreted as an inactive dimeric precursor termed proaerolysin [17], which is eventually activated via proteolysis of the C-terminal peptide [18]. Upon RBD specifically binding to the host glycosylphosphatidyl inositol-anchored proteins, the mature form undergoes drastic conformational changes and oligomerizes into a heptameric quasi-pore on the membrane [16]. Each subunit of the heptamer contributes an amphipathic loop/hairpin to form a 14-stranded β-barrel that inserts into the membrane [19]. Based on the crystal structure of water-soluble dimer and the reconstructed structure of membrane-bound heptamer, a putative model of aerolysin pore formation was proposed [20], which was, however, challenged by succeeding biochemical data [19,21]. Afterward, Degiacomi *et al* hypothesized a swirling membrane-insertion mechanism, based on the pre-pore and quasi-pore structures in addition to molecular dynamics (MD) simulations [16]. Nevertheless, the molecular mechanism of receptor recognition and pore formation for eukaryotic aerolysin members remains largely unknown.

Bioinformatic analysis revealed that the zebrafish *Danio rerio* encodes 16 hypothetical aerolysin-like isoforms [22], which share a 55–98% sequence identity between isoforms over the full-length protein of ~300 residues. Moreover, these isoforms share a sequence identity of ~60% to catfish and lamprey natterin-like proteins, which are hypothetical defense molecules against predators [23,24]. Here, we report the structures of one isoform (NCBI: NP_001013322.1), termed Dln1, in both water-soluble dimeric form (at 1.86 Å) and membrane-bound octameric form (at 20 Å) using X-ray crystallography and electron microscopy (EM), respectively. Crystal structure reveals that each subunit of Dln1 dimer contains an N-terminal β-prism lectin module and a C-terminal aerolysin module, providing the first structural information of a vertebrate aerolysin. The lectin module specifically recognizes the high-mannose glycans that contain a non-reducing terminus of Manα1-2Man or Manα1-3Man, whereas the aerolysin module is responsible for pore formation. The EM structure of membrane-bound octamer presents a quasi-pore state, revealing drastic conformational changes compared with the water-soluble dimer. Combined with MD simulations and biochemical analyses, we propose a putative model for the pore formation of the first vertebrate aerolysin member. Moreover, like human immune protein ZG16p [25] and cyanobacterial anti-HIV protein cyanovirin-N [26], Dln1 also displays a very high affinity toward yeast mannan and gp120 of HIV, suggesting its potential role of defense in zebrafish immune system. These findings increase our knowledge on how a eukaryotic aerolysin-like protein functions as a novel defensive weapon.

Results

Overall structure of the dimeric Dln1

Using the method of single-wavelength anomalous dispersion, we determined the structure of Dln1 at 1.86 Å resolution (Table EV1). Each asymmetric unit contains a homodimer, the two subunits of

which pack against each other in an antiparallel mode with two symmetric dimeric interfaces (Fig 1A), leading to a total buried area of 1,420 Å^2 per subunit. Each dimeric interface is mainly stabilized by 10 hydrogen bonds and one salt bridge (Fig 1B). In fact, Dln1 also exists as a dimer in solution, which was further proved by disulfide-bond cross-linking of the double-mutant S210C-E244C (for more details, see Appendix Fig S1 and legend).

Each subunit, which adopts an elongated shape of 105 × 24 × 24 Å^3, folds into two discrete modules (Appendix Fig S2A). The N-terminal module containing three 4-stranded β-sheets adopts an approximately threefold symmetric β-prism I lectin fold, thus termed lectin module. Structural comparison against the DALI database [27] revealed that this module is most similar to jacalin-related mannose-binding lectins, such as banana *Musa paradisiac* lectin Banlec [28] (PDB 3MIT), red alga *Griffithsia* griffithsin [29] (PDB 3LL0), Jerusalem artichoke *Helianthus tuberosus* heltuba [30] (PDB 1C3K), and human immune protein ZG16p [31] (PDB 3VY7), with a Z-score of 16–28 and a root-mean-square deviation (RMSD) of 1.8–1.9 Å over ~130 Cα atoms, despite sharing a very low sequence homology. The C-terminal module is composed of two distinct β-sandwiches. The β-sandwich at the middle moiety consists of five twisted antiparallel β-sheets with an amphipathic hairpin on one side, whereas the C-terminal β-sandwich comprises a three-stranded antiparallel β-sheet packing against a two-stranded one
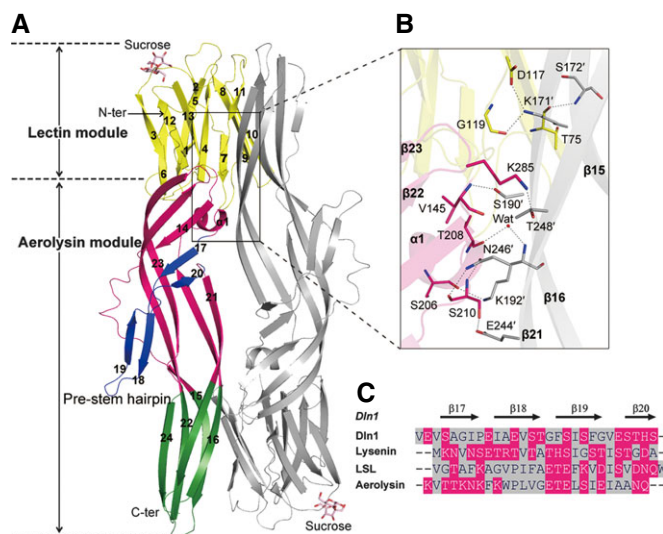

Figure 1. Overall structure of Dln1 dimer.

A Cartoon representation of the Dln1 dimer (PDB 4ZNO). Subunit A is colored in gray. The lectin module of subunit B is colored in yellow, whereas the middle and C-terminal moieties of the aerolysin module are colored in hot pink and green, respectively. The pre-stem hairpin is colored in blue. The bound sucrose molecules are shown as light pink sticks.

B The dimeric interface. Residues involved in dimeric interactions are shown as sticks.

C Multiple-sequence alignment of the pre-stem hairpin (the putative transmembrane region) from different aerolysin members. The members include Dln1, the earthworm *Eisenia foetida* lysenin, the mushroom *Laetiporus sulphureus* lectin (LSL), and *Aeromonas hydrophila* aerolysin. The alignment is generated according to the alternating pattern of hydrophilic and hydrophobic residues by GeneDoc. The hydrophilic and hydrophobic residues are marked in hot pink and gray, respectively.

(Fig 1A). Structural comparison revealed that it resembles aerolysin family proteins, thus we termed it aerolysin module. The top hits include *L. sulphureus* lectin LSL [7] (PDB 1W3A, Z-score 11.6, RMSD 3.07 Å over 148 C_α atoms) and *A. hydrophila* aerolysin [20] (PDB 1PRE, Z-score 5.0, RMSD 3.53 Å over 140 C_α atoms). Similar to previously identified aerolysin members, Dln1 also has a conserved aerolysin fold (Appendix Fig S2B) and an amphipathic pre-stem hairpin that forms the β-barrel [19]. Notably, the aerolysin members share a very low sequence homology, but the pattern of alternative hydrophilic and hydrophobic residues in the pre-stem hairpin is well conserved (Fig 1C).

Remarkably, structural superposition revealed that the strands β15 and β16 buried at the dimeric interface of Dln1 correspond to the β-strands covered by the C-terminal peptide in *A. hydrophila* aerolysin (Fig EV1). This C-terminal peptide, whose proteolysis triggers the activation process, was proposed to protect *A. hydrophila* aerolysin from pore formation by blocking the residues involved in the oligomerization [16]. We speculated that the dimerization of water-soluble Dln1 may provide an alternative mechanism to keep it from oligomerization before binding to the receptor.

Sugar-binding specificity of the lectin module

The lectin module is structurally similar to the jacalin-related mannose-binding lectins, the sugar-binding site of which is usually made up of three exposed loops, termed GG, binding, and recognition loop, respectively [32]. The primary sugar-binding site composed of GG and binding loops are relatively conserved among jacalin-like lectins, whereas the substrate-specific recognition loops vary a lot [33]. In our structure (PDB 4ZNO), the putative sugar-binding site of lectin module is partly occupied by a sucrose, which was used as the cryoprotectant. The residues Gly131, Ser132, Asp133, and Asp135 in the binding loop and Gly15 in the GG loop create a hydrogen bond network with the non-reducing sugar, whereas only one residue Arg87 in the recognition loop has contacts with the reducing sugar (Fig 2A). Notably, Dln1 also possesses a highly conserved $G^{131}XXXD^{135}$ motif, similar to other β-prism lectins [32], indicating that the key residue Asp135 is indispensable for sugar binding.

To define the specific saccharide that binds to Dln1, we applied fluorescein isothiocyanate (FITC)-labeled Dln1 to the glycan array that contains 609 glycan structures (Mammalian Printed Array version 5.2) at the Consortium for Functional Glycomics (CFG, http://www.functionalglycomics.org). A list of top eight candidate structures with a relative fluorescence unit (RFU) above 20,000 from the screening against 200 μg/ml Dln1 is shown in the Appendix Table S1. Structural analysis revealed all these eight candidates are high-mannose glycans from Man-3 to Man-9, six glycans among which constitute a part of Man-9 structure (No. 316) except for Man-5 (No. 214). However, the two representative high-mannose glycan structures Man-5 (No. 214) and Man-9 (No. 316) share a non-reducing terminus of Manα1-2Man or Manα1-3Man (Fig 2B).

In consequence, we detected the binding affinity of Dln1 toward the mannobioses Manα1-2Man and Manα1-3Man, respectively (Fig EV2). Both assays of surface plasmon resonance and isothermal titration calorimetry showed an equilibrium dissociation constant (K_d) of 0.57–1.65 mM comparable to that of β-prism lectin Banlec

toward Manα1-3Man [34]. Moreover, we solved the crystal structures of Dln1 in complex with Manα1-2Man and Manα1-3Man at 1.9 and 2.1 Å, respectively (Fig 2C and D). They both share an overall structure almost identical to that of Dln1 complexed with sucrose, with an RMSD of 0.2–0.4 Å over 730 Cα atoms. In addition, the non-reducing ends of the three disaccharides are stabilized with a same network of hydrogen bonds in the primary sugar-binding site. However, the oxygen atom O2 of the non-reducing mannose of mannobiose has more van der Waals interactions with Dln1 (up to 18–20 atoms in a distance of 3–6 Å), whereas the glucose O2 atom of sucrose points outward, leading to undetectable binding affinity toward Dln1. Combined with the results of glycan array, we conclude that the lectin module adopts a mannose-specific β-prism I fold that prefers the high-mannose glycans.

Putative binding targets of Dln1

The sugar-binding specificity of Dln1 is reminiscent of the potent virus entry inhibitor cyanovirin-N, which favors the high-mannose glycans (Man-8 and Man-9) of glycoproteins on the envelopes of viruses, such as HIV, Ebola, and influenza [35]. In addition, the homologs of Dln1 lectin module, such as griffithsin and BanLec, have also been proved to be potent anti-HIV proteins thanks to their specific binding to high-mannose glycans of gp120 [29,36]. Thus, we determined the binding affinity of Dln1 toward the glycosylated gp120 by ELISA, and revealed a K_d of about 600 nM (Fig 3A), indicating that Dln1 might also be a potential antiviral protein.

As we know, the high-mannose glycans also display on the cell wall of some fungal species, such as *Saccharomyces cerevisiae* and *Candida albicans*, which possess cell-wall mannans branched by α1-2- and α1-3-linked mannose structures [37]. Therefore, we detected the binding affinity of Dln1 toward yeast mannan and revealed a K_d of ~80 nM (Fig 3B). Notably, mutation of the conserved mannose-binding residue Asp135, which contributes two hydrogen bonds to fix O4 and O6 of the non-reducing sugar residue (Fig 2C and D), almost abolished the binding ability (Fig 3B). It implies the primary sugar-binding site, especially the key residue Asp135, is indispensable, in agreement with a previous report [25]. Moreover, binding assays revealed Dln1 specifically adheres to yeast cells and eventually triggers the yeast aggregation (Fig 3C). However, we did not observe significant cell death as long as incubation for 48 h. More interestingly, we found that the recovered Dln1 proteins from the aggregated yeast cells are mainly oligomers that could not be dissociated in sodium dodecyl sulfate (SDS) at 95°C (Fig 3D), indicating that binding to the yeast cell triggers the oligomerization of Dln1. In addition, the sugar-binding residue Asp135 is indispensable for Dln1 binding to yeast cells (Fig 3C and D), suggesting that Dln1 binds to the yeast cells most likely through specific interactions with the cell-wall sugar components. In fact, the binding of Dln1 to yeast cells could be competitively inhibited by the addition of mannan (Appendix Fig S3).

The factors that trigger the oligomerization and pore formation of Dln1

Previous reports suggested that oligomerization of PFTs is usually triggered by a couple of processes/factors, including proteolysis [18], binding to receptors [38] or specific lipids [10], and
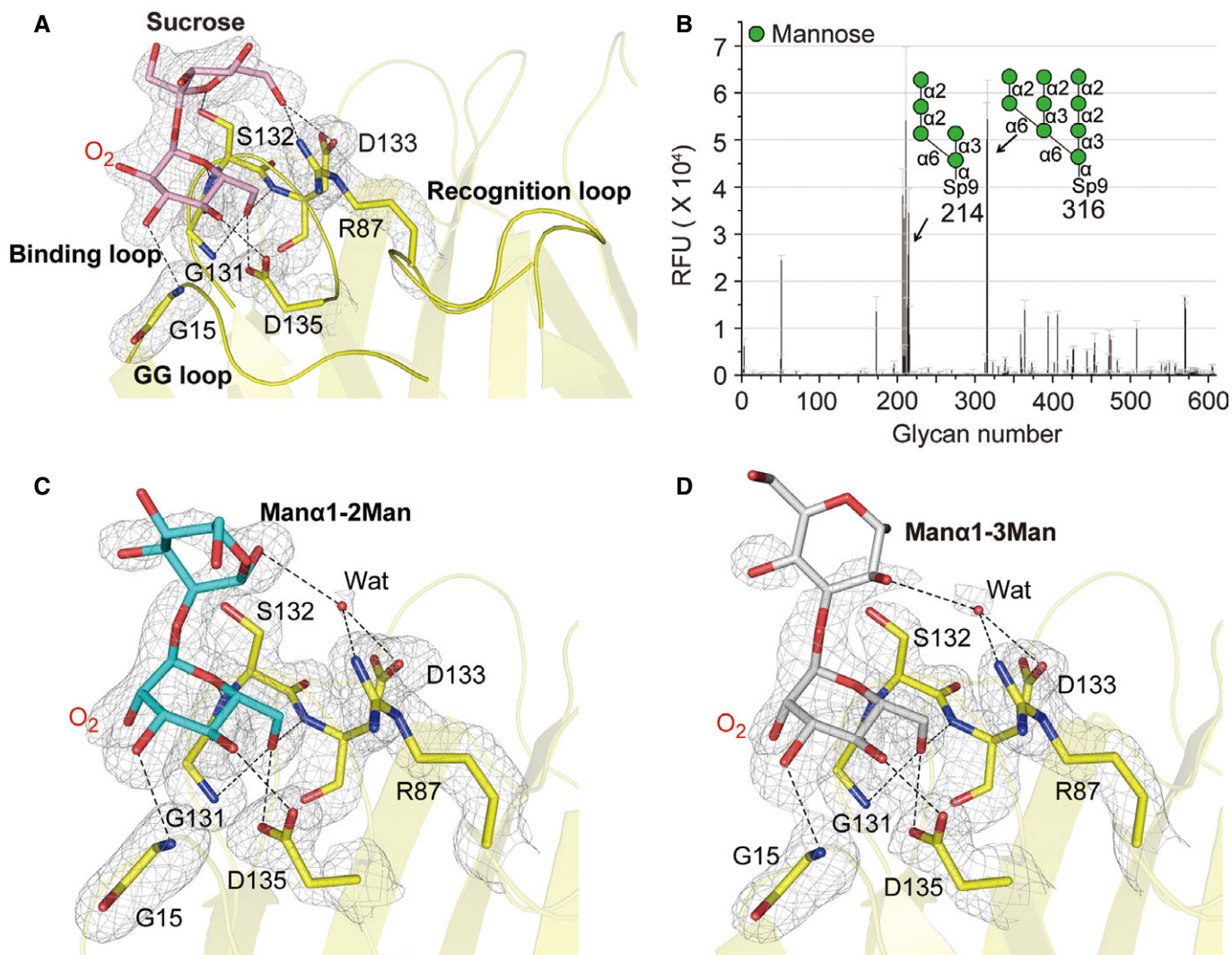
Figure 2. The sugar-binding specificity of the lectin module.

A   A close-up view of the sucrose-binding pocket. The hydrogen-bonding residues with sucrose are shown as yellow sticks, and the sucrose molecule is shown as light pink stick.

B   The glycan binding profile of Dln1. This profile represents FITC-labeled Dln1 at 200 μg/ml screened against 609 printed glycans on Mammalian Printed Array version 5.2 in replicates of six. A list of top 8 hits reacted with a concentration of 200 μg/ml is shown in Appendix Table S1. The two kinds of Dln1-binding glycan structures (No. 214 and 316) are depicted schematically.

C, D   Close-up views of Manα1-2Man- and Manα1-3Man-binding sites. The mannobiose molecules are shown as cyan and gray sticks, respectively. The |Fo|-|Fc| electron density maps of disaccharides and the disaccharide-binding sites are shown as gray mesh and countered at 3.0 σ. The hydrogen-bonding residues are shown as yellow sticks. Polar interactions with the mannobiose are shown as dashed lines.

decrease of pH [39]. For example, the *A. hydrophila* aerolysin undergoes a proteolytic process to remove the C-terminal peptide in prior of oligomerization [18]; however, a corresponding peptide is missing from Dln1 (Fig EV1). Thus, oligomerization of Dln1 should be triggered by a rather different process. To precisely identify the triggering factors, we first analyzed the oligomerization of Dln1 in the presence of mannan or liposomes. In a range of pH values from 7.0 to 9.0, a small fraction of Dln1 formed oligomer in the presence of mannan, whereas the yield of oligomeric Dln1 increased to about fourfold upon the decrease of pH to 6.0 (Fig 4A and Appendix Fig S4A). The liposomes composed of DOPC:DOPE:DOPS at a weight ratio of 9:9:2, which

mimic the components of yeast membrane [40], were also able to promote the oligomerization of Dln1 in a pH-dependent manner (Fig 4A and Appendix Fig S4B).

Furthermore, the liposomes encapsulated by self-quenching carboxyfluorescein were applied to investigate if the oligomerized Dln1 forms a functional transmembrane pore. As shown in Fig 4B, the rate of dye efflux from liposomes displayed a manner dependent on the Dln1 concentration, suggesting that the oligomeric Dln1 indeed penetrated the liposomes. Moreover, upon the decrease of pH from 7.0 to 5.5, the rate of dye release was significantly accelerated (Fig 4C), in agreement with the pH dependency of Dln1 oligomerization (Fig 4A).
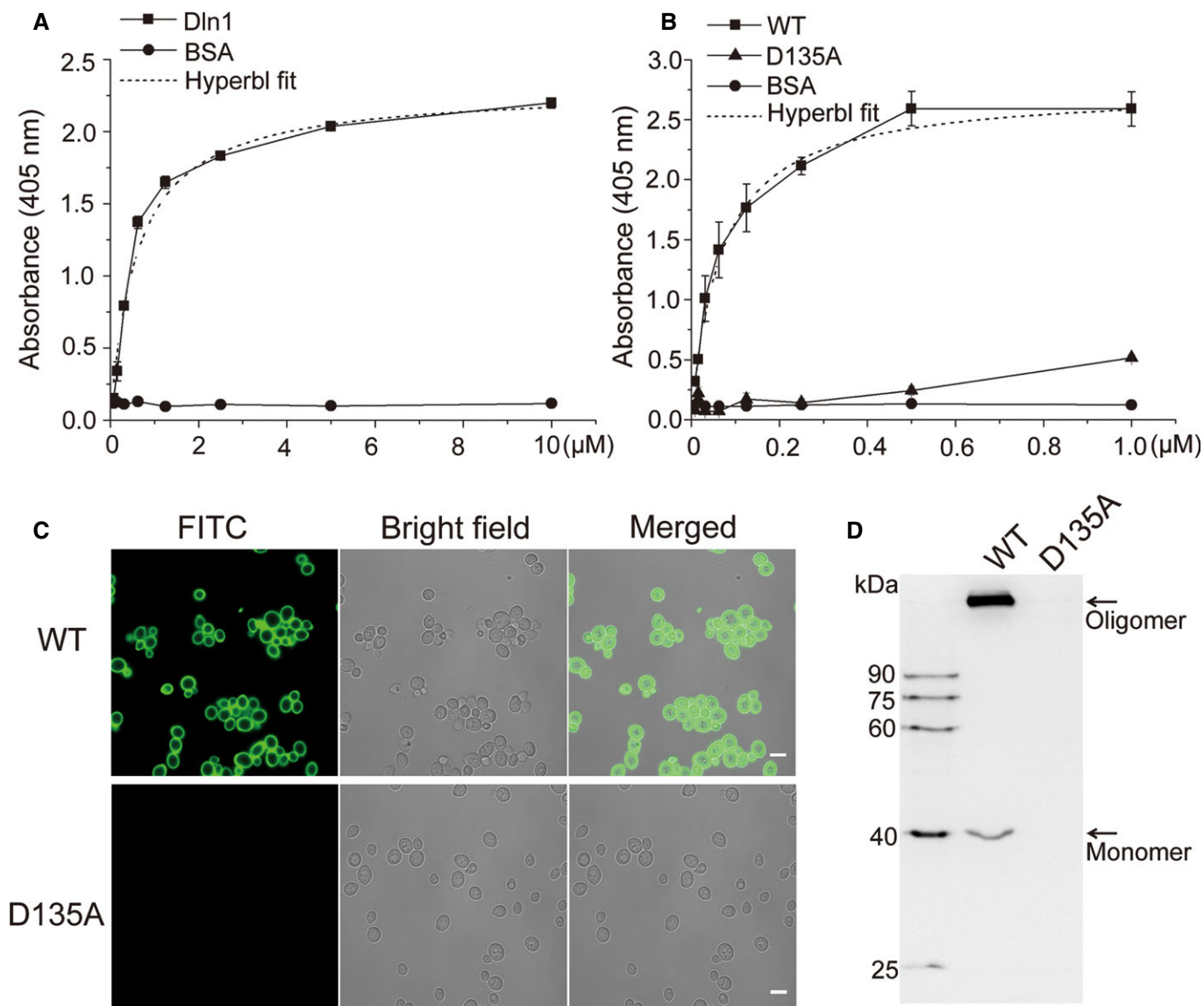
Figure 3. Binding of Dln1 to high-mannose glycans.

A, B   ELISA of Dln1 toward glycosylated gp120 or yeast mannan. BSA was used as the control. Points are averages (± standard error of the mean) of triplicate determinations.

C   Binding of FITC-labeled Dln1 and D135A mutant to *Saccharomyces cerevisiae* cells. Scale bar, 5 µm.

D   Immunoblot analysis of Dln1 and D135A mutant after incubating with *S. cerevisiae* cells. The observed bands represent the cell-bound protein after extensive washing of the yeast cells. The bands corresponding to the monomer and oligomer are highlighted black arrows.

Similar to the previous proposed model of *A. hydrophila* aerolysin [16,20], the water-soluble Dln1 dimer of two antiparallel subunits should be dissociated in prior of oligomerization to allow the alignment of pre-stem hairpins into a β-barrel. According to this hypothesis, the monomeric Dln1 should be able to oligomerize much more easily. Thus, we mutated four residues (Lys171, Ser190, Lys192, and Asn246) at the dimer interface, in addition to the sugar-binding residue Asp135 to avoid the binding of low-yield four-mutant Dln1 to the matrices of Superdex 75™ (GE Healthcare), all to Ala, resulting in a mutant termed Dln1^{M5} for short. In contrast to the wild type, Dln1^{M5} does not form an antiparallel dimer, as confirmed by size-exclusion chromatography and the disulfide-bond cross-linking (Appendix Fig S4C). The circular dichroism spectra indicated that Dln1^{M5} shares a profile of secondary structures similar to the wild type and D135A mutant (Appendix Fig S4D). The yield of Dln1^{M5} oligomers increased to about 50% of the input protein upon the pH decrease to 6.0 or 5.5 (Fig 4D and Appendix Fig S4E), much higher than that of the wild-type Dln1 in the presence of mannan (Fig 4A). Moreover, the oligomerization of Dln1^{M5} is independent of the presence of liposomes (Fig 4D). In consistence, Dln1^{M5} induced the dye efflux from liposomes at a higher velocity compared to the wild type (Fig 4E). Thus, dissociation of the antiparallel Dln1 dimer could indeed significantly accelerate the oligomerization and pore formation. Inhibition assays of dye
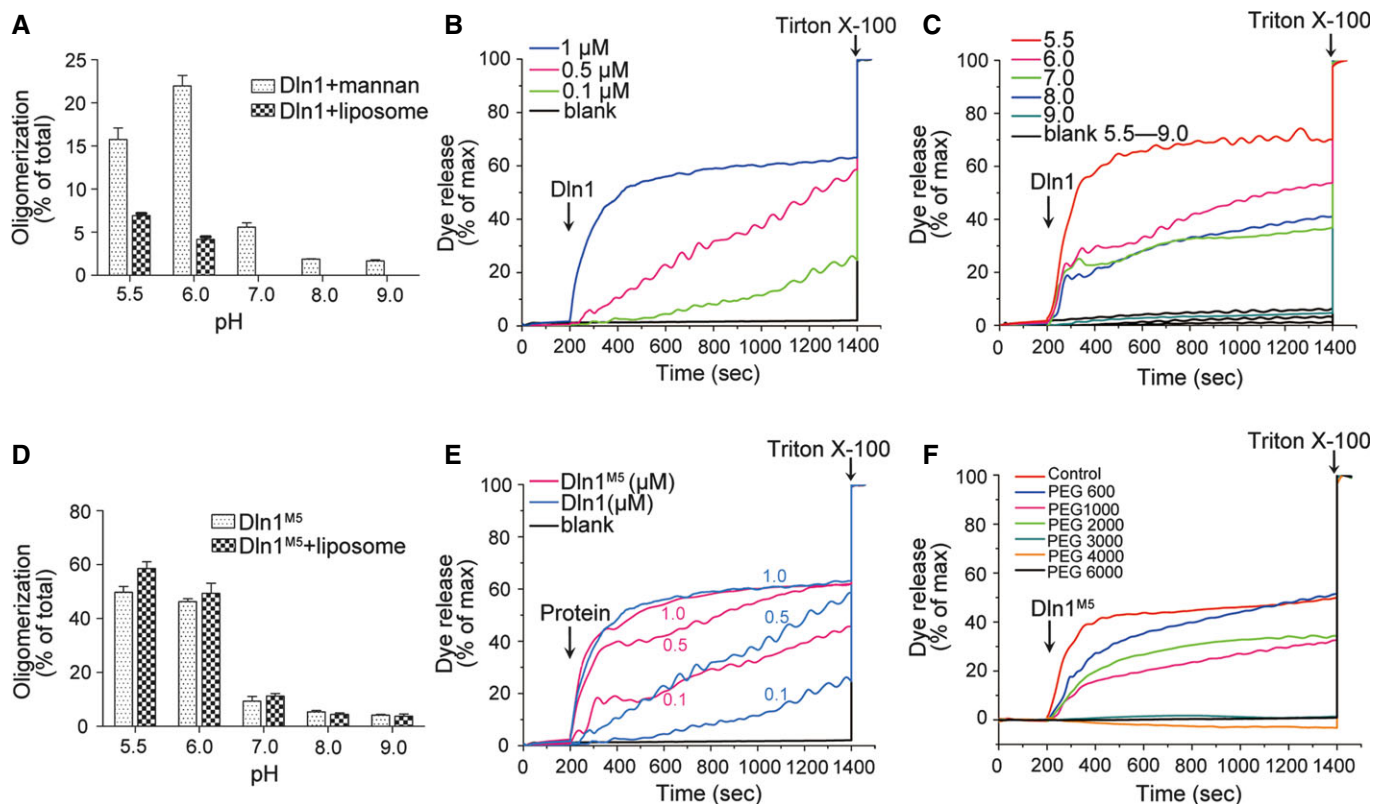
Figure 4.   *In vitro* oligomerization and pore-forming activities of Dln1.

A   Oligomerization of Dln1 in the presence of *S. cerevisiae* mannan or liposomes at different pH values. Histograms are averages (± standard error of the mean) of triplicate determinations.

B, C   Dye release velocity from the liposomes in the presence of Dln1 at different concentrations, and various pH values. Liposomes were incubated with Dln1 of different concentrations at pH 5.5 and 1 μM Dln1 at various pH values, respectively.

D   Oligomerization of Dln1^{M5} with or without liposomes at different pH values. All samples for electrophoresis were prepared with boiling at 95°C for 5 min, and the comparative gels were processed in parallel. The oligomer band was quantified by ImageJ software using the marker band as a sample processing control. The SDS–PAGE profiles of Dln1 oligomerization are shown in Appendix Fig S4. Histograms are averages (± standard error of the mean) of triplicate determinations.

E   Liposomes were treated with Dln1^{M5} or Dln1 of different concentrations at a fixed pH value of 5.5.

F   The inhibition of dye release in presence of 0.5 μM Dln1^{M5} and 25 mM polyethylene glycols (PEG) of different molecular weights at a fixed pH value of 5.5. Dye efflux was monitored in a period of 1,400 s. Triton X-100 at 0.1% was added to completely disrupt liposomes. Dye efflux was measured as a percentage to the maximal release upon addition of Triton X-100. Carboxyfluorescein was loaded in the liposomes for the detection of dye efflux.

Source data are available online for this figure.

efflux suggested the pores on liposomes have a diameter of ~2.8 nm (Fig 4F), as estimated by the size of PEG 3000 [41].

The octameric structure of Dln1

To further investigate the structure of the oligomeric state of Dln1 on membrane, we applied EM to examine Dln1^{M5} incubated with liposomes. The proteins form well-ordered ring-shaped oligomers of ~10 nm in diameter, protruding from liposomes in a square-lattice array (Fig 5A). The side views of the oligomers on liposomes were selected and aligned by utilizing EMAN [42]. The calculated class averages of the side views of these oligomers exhibit an overturn bowl shape with a diameter of 110–120 Å at the mouth and a height of 60–70 Å (Fig 5B).

This protein crystalline pattern on the liposomes encouraged us to investigate the oligomeric structure of Dln1 by electron crystallography. Accordingly, we incubated Dln1^{M5} solution underneath a phospholipid monolayer with the same composition of the liposomes and examined the formation of 2D crystals. We found that Dln1^{M5} readily forms an octameric ring-like structure (Fig 5C). Notably, the single-mutant Dln1^{D135A} also adopts a similar octameric structure on lipid monolayer (Fig 5D); however, we failed to detect the EM structure of the wild-type Dln1. Under the optimal condition, Dln1^{M5} forms well-organized 2D crystals with an area of several square micrometers (Fig 5E). The Fourier transform of EM images of the best 2D crystals have sharp reflection signals at a resolution as high as 20 Å under negative staining conditions. The overall weighted phase residual of the 2D crystals have a smallest value of 16.3° for the *P*4 space group, indicating that the crystals have a fourfold symmetry (Appendix Table S2). Using multiple micrographs of 2D crystals, we calculated the projection density averaging of non-tilted crystals with *P*4 symmetry and
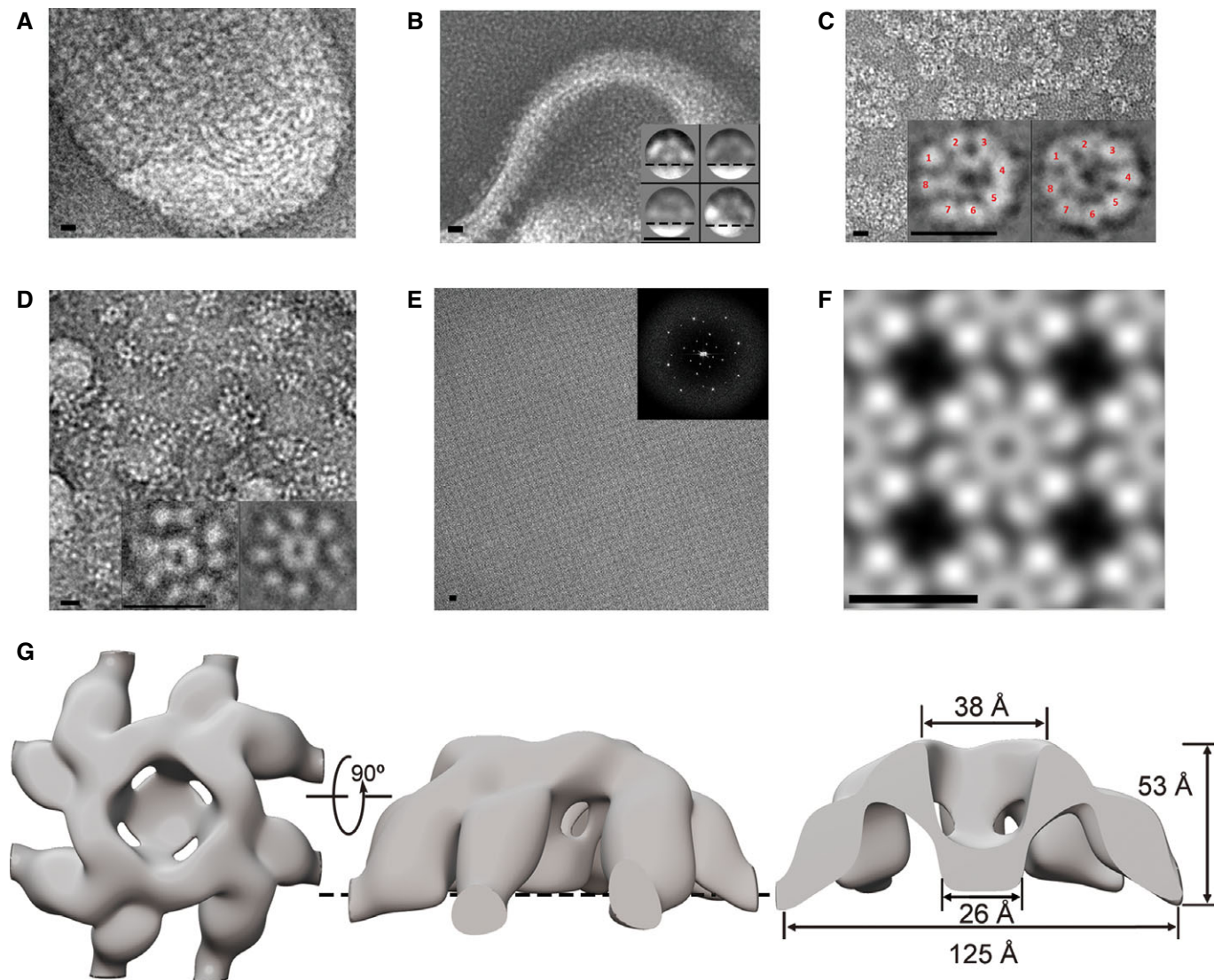
Figure 5. 3D reconstruction of Dln1 octamer.

A   Negative-stain electron microscopy image of Dln1^{M5} in the presence of liposomes.

B   Side views of Dln1^{M5} oligomers attached to the membrane of liposomes. The inset represents the respective class averages.

C, D   Transmission electron microscope micrograph of dispersed ring-like structures of Dln1^{M5} or Dln1^{D135A} oligomers on lipid monolayer. The inset represents a few 2D class averages showing the octamer pattern from some individual rings.

E   EM picture of a negatively stained 2D crystal of Dln1^{M5} on the lipid monolayer. The inset represents the computed diffraction pattern Fourier transform of the image.

F   Projection map with a *P4* symmetry.

G   The top, side, and cut-open views of the 3D reconstruction of Dln1^{M5} octamer at 20 Å resolution are shown as gray surface representation. The surface of the membrane is indicated by dashed lines.

Data information: Scale bars, 10 nm.

found that in each unit cell of the 2D crystal, there is a two-tiered structure with a central ring and outer eightfold spokes (Fig 5F), very similar to the individual octameric rings on the membrane (Fig 5C, inlet). The outer spokes expand to a diameter of approximately 120–125 Å, whereas the central ring has a diameter of about 27–28 Å.

In order to reveal the 3D structure of Dln1 octamer on the phospholipid monolayer, we took EM micrographs of multiple 2D crystals tilted at various angles and performed 3D reconstruction of the 2D crystals at ~20 Å resolution. The 3D density shows the octamer assemblies in an octopus shape with eight feet and a center-hollowed body (Fig 5G). The octamer has an outer diameter of 125 Å and a height of 53 Å, whereas the central hollow has a diameter of 38 Å at the gate and 26 Å at the bottom (Fig 5G), which is comparable to the 2.8-nm diameter of pores on the liposomes (Fig 4F). In accordance with this model, a stain-excluding density between the "bowl" concave and liposome in the averaged side-view images was observed (Fig 5B), revealing that the eight feet of

octopus stand on the phospholipid monolayer (Fig 5G), which was not reconstructed in the EM density map.

To further model the organization of the octamer, we attempted to dock the atomic structure of water-soluble Dln1 into the EM density map. The whole molecule cannot be fit into the density map, as there should be a major conformational change of Dln1 upon insertion into the membrane. We therefore performed docking of the individual modules of Dln1 separately. It is hypothetical that the lectin module is fit into the 3D map, with the sugar-binding surface facing the membrane (Fig 6A), whereas the aerolysin module cannot be fit in the map. It is therefore very likely that drastic conformational changes happen in the aerolysin module that comprises the side wall and mouth of the center-hollowed body of the octopus. This is in agreement with the high flexibility of the aerolysin module that possesses a significantly higher crystallographic B-factor (Fig 6B). The docked model showed that the membrane-bound octamer is composed of eight Dln1 subunits, which are aligned in parallel (Fig 6A), rather than antiparallel in the water-soluble dimeric form. Mass spectrometry analysis of the cross-linked Dln1 in solution also indicated the intermolecular interactions between some symmetric residues pairs, such as K182-K182′, K186-K186′, and K313-K182′ (Appendix Fig S5). These results strongly suggested that the oligomerization of Dln1 should be initiated with the dissociation of the antiparallel dimer followed by

alignment of resulting monomers in parallel. Meanwhile, the pre-stem hairpin of each monomer should be extracted and twisted into a 16-stranded β-barrel (Fig 6A). However, in the reconstructed octamer structure, the center hollow has not completely penetrated the membrane to form a mature pore.

To mimic the details of conformational changes during pore formation, we performed 100-ns MD simulations for the monomeric apo-form and pre-stem hairpin extraction form, respectively. With the lectin module superimposed, the backbone RMSD values of the aerolysin module in pre-stem hairpin extraction form are generally higher than 10 Å, and even reach 25 Å during MD simulation. In contrast, the RMSD values of the monomeric apo-form are maintained at a level lower than 10 Å (Appendix Fig S6). These results suggested that the aerolysin module displays a remarkable flexibility especially upon extraction of the pre-stem hairpin. From each form, 200 representative snapshots with equal time intervals out of the trajectory were superimposed against the original Dln1 structure with the lectin module aligned. Consistent with the EM octamer structure, the superpositions also revealed that large conformational changes make the aerolysin module to bend toward the lectin module upon the extraction of the pre-stem hairpin (Fig 6C). In contrast, the *A. hydrophila* aerolysin module flattens with respect to the RBD to a position almost parallel to the membrane during the pre-pore/pore transition, accompanied by a vertical collapse of
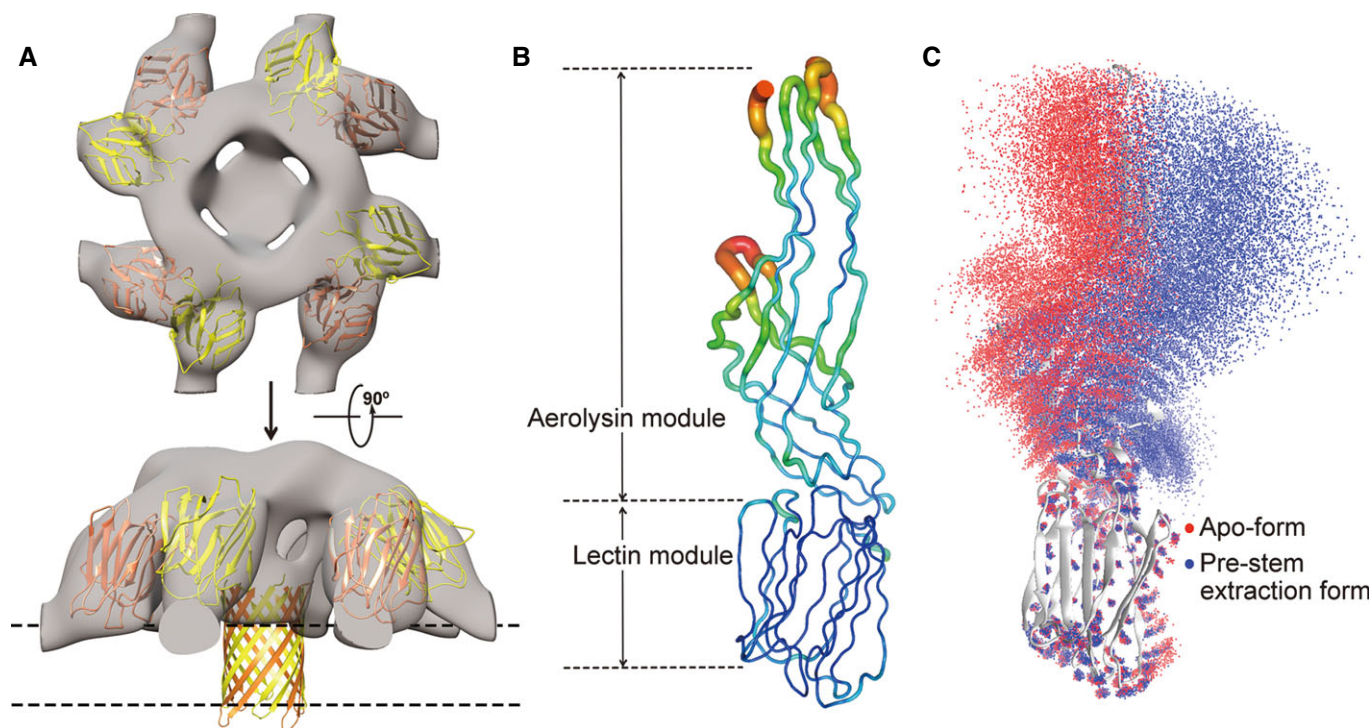

Figure 6. Molecular docking and simulation.

A   Top and side views of eight lectin modules docked to the 20-Å EM map. Due to the moderate resolution of the EM map, the flexible aerolysin module cannot be fit in the map. It is important to notice that this model is only a hypothetical fit. Each pair of the lectin modules is colored in yellow and orange, respectively. The β-barrel of γ-hemolysin (PDB 3B07) was used to mimic the β-barrel backbone of Dln1. The position of the cell membrane is indicated by dashed lines.

B   B-factor of Dln1 subunit B. The mobility is represented by coil thickness from thin (low) to thick (high) and color from blue (low) to red (high). Notably, the pre-stem hairpin and distal moiety of aerolysin module are particularly mobile.

C   Position of C_α atoms along MD simulations of the apo-form (red) and the pre-stem hairpin extraction form (blue) are shown with the lectin modules superimposed (200 structures for each).

the heptamer [16]. The different action modes of the conserved aerolysin module might be due to the diverse RBDs. Together, these findings provide insights into how a eukaryotic aerolysin protein assembles into a pore/quasi-pore.

Discussion

Previous studies on the structure and mechanism of aerolysin family have been focused on the bacterial members [14]. A recent report of the bacterial aerolysin structures has proposed a swirling membrane-insertion mechanism, in which the antiparallel dimers undergo conformational changes to oligomerize into the heptamer, accompanied with a vertical collapse of the complex on the membrane [16]. Proteolysis of the C-terminal peptide initiates the activation process, which includes dissociation of the antiparallel dimer followed by oligomerization and pore formation [16]. However, as the Dln1 lacks a corresponding C-terminal peptide, it should undergo a rather different activation process prior to pore formation.

A putative model for the pore formation of Dln1

Here, we report the first couple of structures of a vertebrate aerolysin-like protein from the zebrafish *D. rerio,* in the water-soluble dimeric form and membrane-bound octameric form. Structural analysis in combination with MD simulations, site-directed mutagenesis, and biochemical assays enable us to have a global view of the allosteric mechanism of a eukaryotic aerolysin protein during pore formation (Fig 7). Upon binding to mannan, a small fraction of Dln1 dimeric proteins form SDS-resistant oligomers in a pH-dependent manner (Fig 4A). The Dln1 structure at pH 5.3 (PDB 5DIO) revealed a hydrogen bond between the residues Glu169 and His264 (Fig EV3A), with the side chains of which orientate differently compared to the structure of Dln1 at pH 7.5 (PDB 4ZNQ). Moreover, in presence of mannan the oligomerization of the double-mutant Dln1$^{E169A-H264A}$ is independent of pH decrease (Fig EV3B). It is possible that the protonation of His264 at acidic pH induces the formation of the hydrogen bond between Glu169 and His264, and eventually promotes the Dln1 oligomerization, in agreement with the previous report of Buckley *et al* [39]. Thus, the process of pore formation is most likely triggered by the recognition of Dln1 lectin module to the glycosylated extracellular receptors on the target cells, which could be accelerated at a microenvironment of relative lower pH and enriched of lipid in the physiological conditions. However, the fact that Dln1 recovered from yeast cells are mainly oligomers strongly indicates there is a missing trigger for the Dln1 oligomerization *in vivo*.

Upon binding to the receptor, the antiparallel dimer undergoes drastic conformational changes to dissociate into transient monomers. Indeed, altering the dimeric interface could significantly promote the oligomerization of Dln1, and moreover, the monomers can autonomously oligomerize independent of binding to mannan/lipid (Fig 4D). Mass spectrometry analysis of chemically cross-linked Dln1^{M5} in solution revealed intermolecular interactions between the aerolysin modules (Appendix Fig S5), which are initially buried at the dimer interface of water-soluble form (Fig EV1). These results strongly suggest the oligomerization of Dln1 needs the dissociation of the antiparallel dimer, which may protect the protein from oligomerization before binding to its receptor. It provides an alternative mechanism distinct from the activation mechanism adopted by the previously reported bacterial aerolysins [14].

After the dissociation of antiparallel dimer, the transient monomers adhered to the exposed glycans of the receptors should be aligned in parallel, as seen from the final octamer EM structure (Fig 5G), and proved by cross-linking of a couple of intermolecular residue pairs, such as K182-K182′, K186-K186′, and K313-K182′ (Appendix Fig S5). Eventually, the parallel aligned Dln1 monomers recruited at the same locus form an octameric pre-pore, different from the heptameric pre-pore of *A. hydrophila* aerolysin [16]. Following the extraction of the pre-stem hairpins, which constitute a twisted β-barrel in a microenvironment enriched of lipid, the protruding aerolysin module of Dln1 gets bent and forms an octopus-like structure (Fig 5G). Finally, eight Dln1 monomers form a
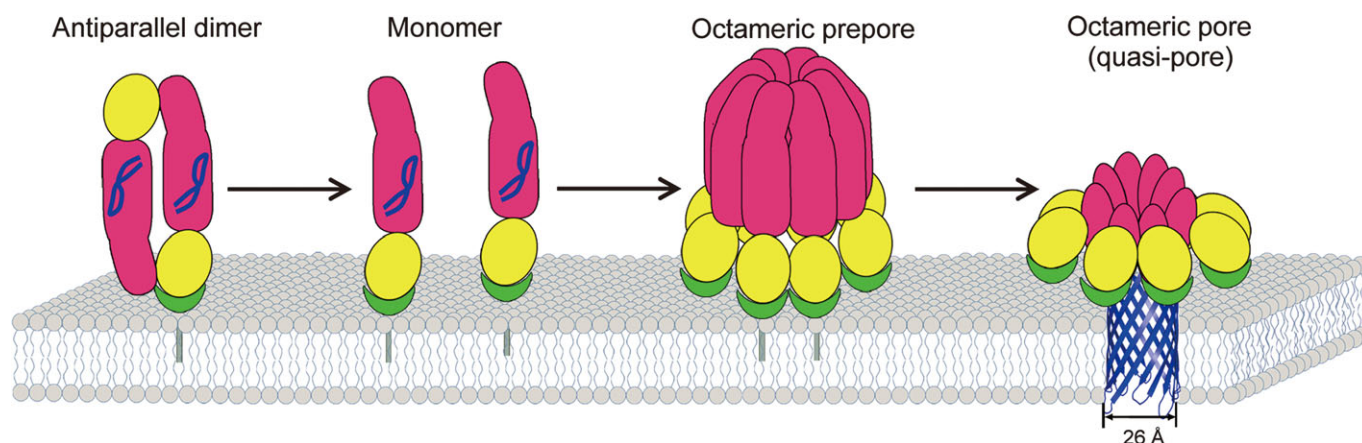

Figure 7. A putative model of Dln1 pore formation.
The lectin module, aerolysin module and receptor are colored in yellow, hot pink, and green, respectively. The membrane is shown in gray. The β-barrel is adopted from that of γ-hemolysin (PDB 3B07).

pore that penetrates the target membrane, as seen from the side view of pores on liposomes (Fig 5B).

In contrast to that in the pre-pore state, the pre-stem hairpin of *A. hydrophila* aerolysin in the quasi-pore state is extracted, leading to the high flexibility and eventually vertical collapse of the aerolysin module [16]. As shown in the octopus-like EM structure (Fig 6A), the collapsed aerolysin module of Dln1 constitutes a part of the side-wall and mouth of the center-hollowed body. Moreover, the 26-Å inner diameter of the pore-like density is comparable to the 2.8-nm transmembrane pore on the liposomes (Fig 4F) and the 25.5-Å β-barrel in diameter of γ-hemolysin octameric pore [43], indicating that this pore-like density is most likely composed of the pre-stem hairpins of Dln1. In addition, the lipid is able to induce the pore formation; however, due to limit of the thickness of lipid monolayer, the center hollow has not completely penetrated the membrane to form a pore. Thus, we propose the membrane-bound Dln1 octamer structure represents a quasi-pore.

Dln1 and isoforms may play a defense role

The specific affinity of Dln1 toward high-mannose glycans, which are abundant on the surface of virus and fungi [35,37], strongly hints its putative defense role. In fact, the homologs of Dln1 lectin module are widespread in plants, and moreover, some of these lectins such as heltuba and griffithsin have been proposed to defend against the invaders of plants [30,44]. Another homolog, the human ZG16p, exhibits high affinity toward the mannan of yeast and pathogenic fungi and has been suggested to attack the invading pathogens in the digestive system [25]. Similar to its homologs in catfish and lamprey [23,24], Dln1 might be also a defense molecule in zebrafish, most likely via forming a transmembrane pore on the target cells similar to the previously reported mammal perforin-2 [6].

A previous phylogenetic analysis has suggested that the aerolysin modules of zebrafish Dlns and *A. hydrophila* aerolysin share a same evolutionary origin [22]. More interestingly, the zebrafish suffers the infection of the aquatic bacteria *A. hydrophila*, the aerolysin of which is one of the most important virulence factors [45]. Thus, we speculate that the aerolysin fold of zebrafish might evolve from the bacterial orthologs. In addition, gene duplication enables the zebrafish genome to harbor as many as 16 isoforms (termed Dln1~16) that share a sequence identity of 55–98% among each other.

In conclusion, here we report the first pair of structures of a vertebrate aerolysin member: the water-soluble dimeric pre-form and the membrane-bound octameric quasi-pore. In combination with a series of site-directed mutagenesis and structure-based computational simulations, we propose a pore-forming process with an activation mechanism distinct from the bacterial members. Our findings also provide insights into a putative immune defense molecule universally utilized by all bony fishes and lamprey.

Materials and Methods

Crystallization and structure determination

The gene (NP_001013322.1) encoding Dln1 was synthesized in Sangon biotech, using an *Escherichia coli* codon preference table and then cloned into the expression vector pET28a with an N-terminal His$_6$-tag. The wild-type Dln1 and all mutants were overexpressed in *Escherichia coli* strain BL21 (DE3) and selenium–selenomethionine (SeMet)-substituted Dln1 was overexpressed in *E. coli* B834 (Novagen). All the proteins were purified with Ni-NTA affinity chromatography followed by gel filtration and analyzed by the circular dichroism spectroscopy with a Jasco-810 spectropolarimeter (Jasco, Easton, MD). All crystals were obtained by hanging-drop diffusion at 16°C. Crystals of the SeMet-substituted protein were obtained from 11% (w/v) polyethylene glycol (PEG) 4000, 0.1 M magnesium chloride, 0.1 M sodium citrate, pH 5.0. The crystal of Dln1–sucrose complex was obtained from 8% (w/v) PEG 6000, 1.0 M lithium chloride, 0.1 M HEPES, pH 7.0, using 30% sucrose supplemented with the reservoir solution as the cryoprotectant. The crystals of Dln1 in complex with Manα1-2Man and Manα1-3Man were obtained by cocrystallization of Dln1 with 100 mM mannobiose against 15% (w/v) PEG 6000, 1.0 M lithium chloride, 0.1 M HEPES, pH 7.5, respectively. The crystal at acidic pH was obtained from 12% (w/v) PEG 4000, 0.2 M ammonium acetate, 0.1 M sodium acetate pH 4.0, and the final pH of the drop is 5.3. After flash-freezing at 100 K in a liquid nitrogen stream, data were collected using beamline 17U with a Q315r CCD (ADSC, MARresearch, Germany) at the Shanghai Synchrotron Radiation Facility (SSRF). The initial model was determined by single-wavelength anomalous dispersion (SAD) phasing method [46]. The AutoSol program implemented in PHENIX [47] was used to locate selenium atoms and to calculate the initial phases, yielding FOM and BAYES-CC values of 0.35 and 42.19, respectively. The initial electron-density maps showed clear features of secondary-structural elements, permitting the building of about 80% of the structure in PHENIX, yielding a model CC of 0.79. The refinement was performed with REFMAC5 [48] and COOT [49]. All final models were evaluated with the program MOLPROBITY [50]. The crystal structures have been deposited in the Protein Data Bank under the PDB entry codes of 4ZNO, 4ZNQ, 4ZNR, and 5DIO. Crystallographic parameters were listed in Table EV1. All structure figures were prepared with PyMOL (http://www.pymol.org/).

Glycan chip assay

Purified Dln1 was labeled with fluorescein isothiocyanate (FITC) following the manufacturer's instructions (Sigma). FITC-labeled Dln1 was sent to the Consortium for Functional Glycomics for analysis against 609 glycans on the mammalian glycan screen version 5.2 in replicates of 6. The FITC-labeled Dln1 was used at a concentration of 2, 20, and 200 μg/ml for screening, respectively, following the CFG protocol at http://www.functionalglycomics.org.

Surface plasmon resonance (SPR) assays

All SPR experiments were performed in phosphate-buffered saline (PBS), pH 7.4, at 25°C using a Biacore 3000 instrument (GE Healthcare). Solutions with different concentrations of mannobiose were serially injected for 2 min over the sensor chips CM with immobilized protein and the blank at the flow rate of 30 μl/min. Then, the sensor chip surface was regenerated after washing for 3 min with PBS. The specific binding data were fitted with the liner fit and steady-state affinity mode using the Biacore evaluation software.

Isothermal titration calorimetry (ITC) assays

The purified Dln1 proteins were exhaustively dialyzed against PBS buffer, pH 7.4. The data were collected on MicroCal iTC200 titration microcalorimeter (GE Healthcare) at 25°C by injecting an initial 0.4 μl aliquot and the following 19 consecutive 2 μl aliquots. The 200 μl Dln1 proteins at a concentration of 80 μM was loaded into the sample cell while the injection syringe was loaded with 40 μl of different disaccharides at a concentration of 15 mM.

Binding of Dln1 to yeast mannan and gp120 of HIV

The mannan and gp120 binding assays were carried out as described previously [26]. About 50 μl *S. cerevisiae* mannan (Sigma) and glycosylated gp120 (enzyme) at a concentration of 40 and 2 μg/ml in PBS buffer, pH 7.4, were used to coat the microplate, respectively. About 100 μl of 0.5-log serial dilutions of Dln1 was added into triplicate wells and incubated at 25°C for 3 h; BSA was used as the control. The 1:5,000 diluted anti-Dln1 polyclonal antibody raised in core facility center of Wuhan Institute of Virology and HRP-conjugated goat anti-rabbit IgG (W401B, Promega) were employed to detect the binding Dln1. The wells were washed five times with PBST (PBS, pH 7.4, supplemented with 1% Tween-20) between every two steps to remove the remaining protein and antibody. The EL-P-NPP Chromogenic Reagent Kit (Sangon biotech) was applied to monitor the absorbance at 405 nm using an ELX800 Universal Microplate Reader (Bio-Tek Instruments, Inc.).

Binding of Dln1 to yeast cells

FITC-labeled Dln1, the D135A mutant, and bovine serum album (5 μM for each) in PBS were incubated with yeast cells (10^8 cells/ml) at 25°C for 3 h, respectively. Then, the yeast cells were washed and resuspended in PBS, pH 7.4, and the suspensions were observed with confocal laser scanning microscope (Zeiss LSM510). The inhibition of Dln1 binding to yeast cells was performed by incubation the Dln1 with yeast cells in presence of yeast mannan at different concentrations.

The yeast cells incubated with Dln1 or the D135A mutant were analyzed by 10% SDS polyacrylamide gel electrophoresis (SDS–PAGE) followed by Western blotting using 1:5,000 diluted anti-Dln1 polyclonal antibody raised in core facility center of Wuhan Institute of Virology, and HRP-conjugated goat anti-rabbit IgG (W401B, Promega).

Dln1 oligomerization and dye leakage assays

The liposomes composed of DOPC, DOPE and DOPS at a ratio of 9:9:2 in weight were prepared as described previously [51]. Dln1 at 0.35 mg/ml was incubated with the liposomes at 0.17 mg/ml or mannan at 1.5 mg/ml in the buffer of different pH values at 25°C for 1 h to allow oligomerization. Then, the protein samples were separated on 10% SDS–PAGE. The comparative gels were processed in parallel. All results were repeated for three times. The same procedure was used for the Dln1 mutants as mentioned above. The oligomer band was quantified by ImageJ software (http://imagej.nih.gov/ij/) with the average of triplicate detections, using the marker band as a sample processing control. For dye leakage

assays, release of carboxyfluorescein (Sigma) from carboxyfluorescein-loaded liposomes (10 μM lipids) was measured over time on a spectrofluorometer (F-2700, Hitachi) with an excitation and emission wavelength of 480 and 517 nm, respectively. The assays were performed in the buffer of different pH values. The buffer contained 100 mM NaCl and 50 mM of one of the following buffers: MES in the pH range of 5.5–6.0, Tris–Cl for pH values 7.0–8.0, and bicine pH 9.0.

Negative-stain electron microscopy

Liposomes at 0.2 mg/ml were incubated with 0.4 mg/ml Dln1^{M5} at 25°C for 2 h. The samples were stained with uranyl acetate solution (~2% w/v) and examined by the FEI Tecnai 12 electron microscope with an accelerating voltage of 120 kV at appropriate magnification and defocus. The electron micrographs were recorded on Gatan US4000 4Kx4K CCD.

Generation of 2D crystal on lipid monolayer

The Dln1^{M5} or Dln1^{D135A} at 0.2 mg/ml in 100 mM NaCl, 50 mM MES, pH 5.5, was pipetted into the Teflon block wells, and ~1 μl phospholipid mixture (DOPC:DOPE:DOPS with weight ratio of 9:9:2) at 0.1 mg/ml was placed on the top of Dln1 solution. After incubation at 4°C for 5–6 days, the 2D crystals of Dln1 together with lipid monolayer would be absorbed onto the EM grid. The negatively stained samples were examined in the same manner as liposomes. The electron micrographs were recorded on a Gatan US4000 4Kx4K CCD.

3D reconstruction and docking

In total, 45 images with tilt angles ranging from 0 to 40° were processed in 2dx software package, based on the MRC program [52,53]. For each single-image processing in 2dx_image, projection map was generated by MRC and CCP4 programs and tilt angle was determined by program CTFTILT. With ALLSPACE employed, the space group was identified as *P*4 (Appendix Table S3). In order to reconstruct the 3D structure, the tilted images were aligned in 2dx_merge according to their angles. Ultimately, the overall weighted phase residual for *P*4 symmetry is 16.3° out to 20 Å resolution (Appendix Table S2), while the overall weighted R factor is 0.228 (< 0.4), which are well acceptable in 2dx software system. The EM density map has been deposited in the Electron Microscopy Data Bank under the accession number of EMD-3244. The 6 Å resolution maps for the eight lectin domains were simulated from the X-ray crystal model (4ZNO) and then docked into the 20 Å resolution EM map in UCSF Chimera [54], and subsequently, the docking result was refined by fit-in-map command to make it nicely fitted, with cross-correlation coefficient (CCC) of 0.79.

Molecular dynamic (MD) stimulation

MD simulations were performed for monomeric Dln1 in the apo-form (PDB 4ZNO) and the pre-stem loop extraction state, respectively. The apo-form structure was taken from (PDB 4ZNO), while the structure of the pre-stem loop extraction state was obtained from the apo-form structure by rigid-body modeling with the xplor-NIH

package [55,56]. Simulations were performed using the GROMACS-4.5.5 package [57] and the Amber03 force field [58]. The systems were placed in a TIP3P [59] water-filled dodecahedral box with 115 Na^+ and 116 Cl^- ions to neutralize the systems and to create an ionic concentration of 0.15 M. The other parameters were the same as those in the canonical MD simulation of human vinculin in the work of Peng *et al* [60]. The production run for each simulation was 100 ns. Structure visualization was performed with VMD [61].

Cross-linking mass spectrometry (CXMS)

The ^{14}N- and ^{15}N-labeled Dln1^{M5} were mixed at 1:1 ratio at a protein concentration of 25 μM. Then, the mixtures were cross-linked with the indicated amount BS^3 or disuccinimidyl suberate (protein: DSS with a molar ratio of 1:50) at room temperature for 1 h. As previously described [62], after being quenched with 20 mM NH$_4$HCO$_3$, the resulting products were precipitated and digested with trypsin. The LC-MS/MS analysis was performed on an Easy-nLC 1000 HPLC coupled to a Q Exactive-Orbitrap mass spectrometer (Thermo Fisher Scientific) [62]. Cross-linked ^{14}N-peptides were identified using pLink [63] with a FDR of 5% and *E*-value < 0.001. We also required the cross-linked site pairs to have a best *E*-value < 1×10^{-8}. Inter-molecular cross-links were determined as previously described [64–66]. Through manual evaluation, a cross-linked site pair was assigned to be inter-molecular ones when the intensities of its ^{14}N-^{15}N and ^{15}N-^{14}N forms were above 0.6-fold of its ^{14}N-^{14}N form.

Expanded View for this article is available online.

Author contributions

NJ, NL, HWW, YC, and CZZ conceived and designed the experiments. NJ, NL, HS, LLC, JP, and YHD performed the experiments. NJ, NL, WC, YLJ, YZ, HWW, YC, and CZZ analyzed the data. HW, ZHZ, XW, GC, JFW, MQD, and ZZ contributed reagents/materials/analysis tools. NJ, HWW, YC, and CZZ wrote the manuscript.

Conflict of interest

The authors declare that they have no conflict of interest.

References

1. Bischofberger M, Gonzalez MR, van der Goot FG (2009) Membrane injury by pore-forming proteins. *Curr Opin Cell Biol* 21: 589–595

2. Parker MW, Feil SC (2005) Pore-forming protein toxins: from structure to function. *Prog Biophys Mol Biol* 88: 91–142

3. Iacovache I, Bischofberger M, van der Goot FG (2010) Structure and assembly of pore-forming proteins. *Curr Opin Struct Biol* 20: 241–246

4. Kroemer G, Galluzzi L, Brenner C (2007) Mitochondrial membrane permeabilization in cell death. *Physiol Rev* 87: 99–163

5. Lashuel HA, Lansbury PT Jr (2006) Are amyloid diseases caused by protein aggregates that mimic bacterial pore-forming toxins? *Q Rev Biophys* 39: 167–201

6. McCormack R, de Armas LR, Shiratsuchi M, Ramos JE, Podack ER (2013) Inhibition of intracellular bacterial replication in fibroblasts is dependent on the perforin-like protein (perforin-2) encoded by macrophage-expressed gene 1. *J Innate Immun* 5: 185–194

7. Mancheno JM, Tateno H, Goldstein IJ, Martinez-Ripoll M, Hermoso JA (2005) Structural analysis of the *Laetiporus sulphureus* hemolytic pore-forming lectin in complex with sugars. *J Biol Chem* 280: 17251–17259

8. Sousa MV, Richardson M, Fontes W, Morhy L (1994) Homology between the seed cytolysin enterolobin and bacterial aerolysins. *J Protein Chem* 13: 659–667

9. Sher D, Fishman Y, Zhang M, Lebendiker M, Gaathon A, Mancheno JM, Zlotkin E (2005) Hydralysins, a new category of beta-pore-forming toxins in cnidaria. *J Biol Chem* 280: 22847–22855

10. De Colibus L, Sonnen AF, Morris KJ, Siebert CA, Abrusci P, Plitzko J, Hodnik V, Leippe M, Volpi E, Anderluh G *et al* (2012) Structures of lysenin reveal a shared evolutionary origin for pore-forming proteins and its mode of sphingomyelin recognition. *Structure* 20: 1498–1507

11. Galinier R, Portela J, Mone Y, Allienne JF, Henri H, Delbecq S, Mitta G, Gourbal B, Duval D (2013) Biomphalysin, a new beta pore-forming toxin involved in *Biomphalaria glabrata* immune defense against *Schistosoma mansoni*. *PLoS Pathog* 9: e1003216

12. Xiang Y, Yan C, Guo X, Zhou K, Li S, Gao Q, Wang X, Zhao F, Liu J, Lee WH *et al* (2014) Host-derived, pore-forming toxin-like protein and trefoil factor complex protects the host against microbial infection. *Proc Natl Acad Sci USA* 111: 6702–6707

13. Sher D, Fishman Y, Melamed-Book N, Zhang M, Zlotkin E (2008) Osmotically driven prey disintegration in the gastrovascular cavity of the green hydra by a pore-forming protein. *FASEB J* 22: 207–214

14. Knapp O, Stiles B, Popoff MR (2010) The aerolysin-like toxin family of cytolytic, pore-forming toxins. *Open Toxinol J* 3: 53–68

15. Leone P, Bebeacua C, Opota O, Kellenberger C, Klaholz B, Orlov I, Cambillau C, Lemaitre B, Roussel A (2015) X-ray and Cryo-electron microscopy structures of monalysin pore-forming toxin reveal multimerization of the pro-form. *J Biol Chem* 290: 13191–13201

16. Degiacomi MT, Iacovache I, Pernot L, Chami M, Kudryashev M, Stahlberg H, van der Goot FG, Dal Peraro M (2013) Molecular assembly of the aerolysin pore reveals a swirling membrane-insertion mechanism. *Nat Chem Biol* 9: 623–629

17. Hardie KR, Schulze A, Parker MW, Buckley JT (1995) Vibrio spp. secrete proaerolysin as a folded dimer without the need for disulphide bond formation. *Mol Microbiol* 17: 1035–1044

18. Howard SP, Buckley JT (1985) Activation of the hole-forming toxin aerolysin by extracellular processing. *J Bacteriol* 163: 336–340

19. Iacovache I, Paumard P, Scheib H, Lesieur C, Sakai N, Matile S, Parker MW, van der Goot FG (2006) A rivet model for channel formation by aerolysin-like pore-forming toxins. *EMBO J* 25: 457–466

20. Parker MW, Buckley JT, Postma JP, Tucker AD, Leonard K, Pattus F, Tsernoglou D (1994) Structure of the aeromonas toxin proaerolysin in its water-soluble and membrane-channel states. *Nature* 367: 292–295

21. Diep DB, Nelson KL, Raja SM, Pleshak EN, Buckley JT (1998) Glyco-sylphosphatidylinositol anchors of membrane glycoproteins are binding

determinants for the channel-forming toxin aerolysin. *J Biol Chem* 273: 2355–2360

22. Szczesny P, Iacovache I, Muszewska A, Ginalski K, van der Goot FG, Grynberg M (2011) Extending the aerolysin family: from bacteria to vertebrates. *PLoS ONE* 6: e20349

23. Tamura S, Yamakawa M, Shiomi K (2011) Purification, characterization and cDNA cloning of two natterin-like toxins from the skin secretion of oriental catfish *Plotosus lineatus. Toxicon* 58: 430–438

24. Xue Z, Liu X, Pang Y, Yu T, Xiao R, Jin M, Han Y, Su P, Wang J, Lv L *et al* (2012) Characterization, phylogenetic analysis and cDNA cloning of natterin-like gene from the blood of lamprey, *Lampetra japonica. Immunol Lett* 148: 1–10

25. Tateno H, Yabe R, Sato T, Shibazaki A, Shikanai T, Gonoi T, Narimatsu H, Hirabayashi J (2012) Human ZG16p recognizes pathogenic fungi through non-self polyvalent mannose in the digestive system. *Glycobiology* 22: 210–220

26. Boyd MR, Gustafson KR, McMahon JB, Shoemaker RH, O'Keefe BR, Mori T, Gulakowski RJ, Wu L, Rivera MI, Laurencot CM *et al* (1997) Discovery of cyanovirin-N, a novel human immunodeficiency virus-inactivating protein that binds viral surface envelope glycoprotein gp120: potential applications to microbicide development. *Antimicrob Agents Chemother* 41: 1521–1530

27. Holm L, Rosenstrom P (2010) Dali server: conservation mapping in 3D. *Nucleic Acids Res* 38: W545–W549

28. Sharma A, Vijayan M (2011) Influence of glycosidic linkage on the nature of carbohydrate binding in beta-prism I fold lectins: an X-ray and molecular dynamics investigation on banana lectin-carbohydrate complexes. *Glycobiology* 21: 23–33

29. Moulaei T, Shenoy SR, Giomarelli B, Thomas C, McMahon JB, Dauter Z, O'Keefe BR, Wlodawer A (2010) Monomerization of viral entry inhibitor griffithsin elucidates the relationship between multivalent binding to carbohydrates and anti-HIV activity. *Structure* 18: 1104–1115

30. Bourne Y, Zamboni V, Barre A, Peumans WJ, Van Damme EJ, Rouge P (1999) Helianthus tuberosus lectin reveals a widespread scaffold for mannose-binding lectins. *Structure* 7: 1473–1482

31. Kanagawa M, Liu Y, Hanashima S, Ikeda A, Chai W, Nakano Y, Kojima-Aikawa K, Feizi T, Yamaguchi Y (2014) Structural basis for multiple sugar recognition of jacalin-related human ZG16p lectin. *J Biol Chem* 289: 16954–16965

32. Meagher JL, Winter HC, Ezell P, Goldstein IJ, Stuckey JA (2005) Crystal structure of banana lectin reveals a novel second sugar binding site. *Glycobiology* 15: 1033–1042

33. Jeyaprakash AA, Srivastav A, Surolia A, Vijayan M (2004) Structural basis for the carbohydrate specificities of artocarpin: variation in the length of a loop as a strategy for generating ligand specificity. *J Mol Biol* 338: 757–770

34. Mo H, Winter HC, Van Damme EJ, Peumans WJ, Misaki A, Goldstein IJ (2001) Carbohydrate binding properties of banana (*Musa acuminata*) lectin I. Novel recognition of internal alpha1,3-linked glucosyl residues. *Eur J Biochem* 268: 2609–2615

35. Barrientos LG, Gronenborn AM (2005) The highly specific carbohydrate-binding protein cyanovirin-N: structure, anti-HIV/Ebola activity and possibilities for therapy. *Mini Rev Med Chem* 5: 21–31

36. Swanson MD, Winter HC, Goldstein IJ, Markovitz DM (2010) A lectin isolated from bananas is a potent inhibitor of HIV replication. *J Biol Chem* 285: 8646–8655

37. Cummings RD, Doering TL (2009) Fungi. *Essentials of Glycobiology*, 2nd edn. New York: Cold Spring Harbor

38. Abrami L, van Der Goot FG (1999) Plasma membrane microdomains act as concentration platforms to facilitate intoxication by aerolysin. *J Cell Biol* 147: 175–184

39. Buckley JT, Wilmsen HU, Lesieur C, Schulze A, Pattus F, Parker MW, van der Goot FG (1995) Protonation of histidine-132 promotes oligomerization of the channel-forming toxin aerolysin. *Biochemistry* 34: 16450–16455

40. van der Rest ME, Kamminga AH, Nakano A, Anraku Y, Poolman B, Konings WN (1995) The plasma membrane of *Saccharomyces cerevisiae*: structure, function, and biogenesis. *Microbiol Rev* 59: 304–322

41. Merzlyak PG, Yuldasheva LN, Rodrigues CG, Carneiro CM, Krasilnikov OV, Bezrukov SM (1999) Polymeric nonelectrolytes to probe pore geometry: application to the alpha-toxin transmembrane channel. *Biophys J* 77: 3023–3033

42. Ludtke SJ, Baldwin PR, Chiu W (1999) EMAN: semiautomated software for high-resolution single-particle reconstructions. *J Struct Biol* 128: 82–97

43. Yamashita K, Kawai Y, Tanaka Y, Hirano N, Kaneko J, Tomita N, Ohta M, Kamio Y, Yao M, Tanaka I (2011) Crystal structure of the octameric pore of staphylococcal gamma-hemolysin reveals the beta-barrel pore formation mechanism by two components. *Proc Natl Acad Sci USA* 108: 17314–17319

44. Mori T, O'Keefe BR, Sowder RC II, Bringans S, Gardella R, Berg S, Cochran P, Turpin JA, Buckheit RW Jr, McMahon JB *et al* (2005) Isolation and characterization of griffithsin, a novel HIV-inactivating protein, from the red alga Griffithsia sp. *J Biol Chem* 280: 9345–9353

45. Rodriguez I, Novoa B, Figueras A (2008) Immune response of zebrafish (*Danio rerio*) against a newly isolated bacterial pathogen *Aeromonas hydrophila. Fish Shellfish Immunol* 25: 239–249

46. Brodersen DE, de la Fortelle E, Vonrhein C, Bricogne G, Nyborg J, Kjeldgaard M (2000) Applications of single-wavelength anomalous dispersion at high and atomic resolution. *Acta Crystallogr D Biol Crystallogr* 56: 431–441

47. Adams PD, Afonine PV, Bunkoczi G, Chen VB, Davis IW, Echols N, Headd JJ, Hung LW, Kapral GJ, Grosse-Kunstleve RW *et al* (2010) PHENIX: a comprehensive Python-based system for macromolecular structure solution. *Acta Crystallogr D Biol Crystallogr* 66: 213–221

48. Murshudov GN, Vagin AA, Dodson EJ (1997) Refinement of macromolecular structures by the maximum-likelihood method. *Acta Crystallogr D Biol Crystallogr* 53: 240–255

49. Emsley P, Cowtan K (2004) Coot: model-building tools for molecular graphics. *Acta Crystallogr D Biol Crystallogr* 60: 2126–2132

50. Davis IW, Leaver-Fay A, Chen VB, Block JN, Kapral GJ, Wang X, Murray LW, Arendall WB III, Snoeyink J, Richardson JS *et al* (2007) MolProbity: all-atom contacts and structure validation for proteins and nucleic acids. *Nucleic Acids Res* 35: W375–W383

51. Mukherjee S, Zheng H, Derebe MG, Callenberg KM, Partch CL, Rollins D, Propheter DC, Rizo J, Grabe M, Jiang QX *et al* (2014) Antibacterial membrane attack by a pore-forming intestinal C-type lectin. *Nature* 505: 103–107

52. Gipson B, Zeng X, Zhang ZY, Stahlberg H (2007) 2dx–user-friendly image processing for 2D crystals. *J Struct Biol* 157: 64–72

53. Gipson B, Zeng X, Stahlberg H (2007) 2dx_merge: data management and merging for 2D crystal images. *J Struct Biol* 160: 375–384

54. Pettersen EF, Goddard TD, Huang CC, Couch GS, Greenblatt DM, Meng EC, Ferrin TE (2004) UCSF Chimera—a visualization system for exploratory research and analysis. *J Comput Chem* 25: 1605–1612

55. Schwieters CD, Kuszewski JJ, Tjandra N, Clore GM (2003) The Xplor-NIH NMR molecular structure determination package. *J Magn Reson* 160: 65−73

56. Schwieters CD, Kuszewski JJ, Clore GM (2006) Using Xplor−NIH for NMR molecular structure determination. *Prog Nucl Magn Reson Spectrosc* 48: 47−62

57. Hess B, Kutzner C, van der Spoel D, Lindahl E (2008) GROMACS 4: algorithms for highly efficient, load-balanced, and scalable molecular simulation. *J Chem Theory Comput* 4: 435−447

58. MacKerell AD, Bashford D, Bellott M, Dunbrack RL, Evanseck JD, Field MJ, Fischer S, Gao J, Guo H, Ha S *et al* (1998) All-atom empirical potential for molecular modeling and dynamics studies of proteins. *J Phys Chem B* 102: 3586−3616

59. Jorgensen WL, Chandrasekhar J, Madura JD, Impey RW, Klein ML (1983) Comparison of simple potential functions for simulating liquid water. *J Chem Phys* 79: 926−935

60. Peng JH, Zhang ZY (2014) Simulating large-scale conformational changes of proteins by accelerating collective motions obtained from principal component analysis. *J Chem Theory Comput* 10: 3449−3458

61. Humphrey W, Dalke A, Schulten K (1996) VMD: visual molecular dynamics. *J Mol Graph* 14: 33−38, 27-38

62. Liu XM, Sun LL, Hu W, Ding YH, Dong MQ, Du LL (2015) ESCRTs cooperate with a selective autophagy receptor to mediate vacuolar targeting of soluble cargos. *Mol Cell* 59: 1035−1042

63. Yang B, Wu YJ, Zhu M, Fan SB, Lin J, Zhang K, Li S, Chi H, Li YX, Chen HF *et al* (2012) Identification of cross-linked peptides from complex samples. *Nat Methods* 9: 904−906

64. Taverner T, Hall NE, O'Hair RA, Simpson RJ (2002) Characterization of an antagonist interleukin-6 dimer by stable isotope labeling, cross-linking, and mass spectrometry. *J Biol Chem* 277: 46487−46492

65. Merkley ED, Baker ES, Crowell KL, Orton DJ, Taverner T, Ansong C, Ibrahim YM, Burnet MC, Cort JR, Anderson GA *et al* (2013) Mixed-isotope labeling with LC-IMS-MS for characterization of protein-protein interactions by chemical cross-linking. *J Am Soc Mass Spectrom* 24: 444−449

66. Petrotchenko EV, Serpa JJ, Makepeace KA, Brodie NI, Borchers CH (2014) (14)N(15)N DXMSMS Match program for the automated analysis of LC/ESI-MS/MS crosslinking data from experiments using (15)N metabolically labeled proteins. *J Proteomics* 109: 104−110